

Article

The Multi-Scale Temporal Variability of Extreme Precipitation in the Source Region of the Yellow River

Peng Jiang ^{1,2}, Zhongbo Yu ^{1,2,*}, Feifei Yuan ¹  and Kumud Acharya ²

¹ State Key Laboratory of Hydrology-Water Resources and Hydraulic Engineering, Hohai University, Nanjing 210098, China; peng.jiang@dri.edu or peng.hydro@gmail.com (P.J.); ffei.yuan@gmail.com (F.Y.)

² Division of Hydrologic Sciences, Desert Research Institute, Las Vegas, NV 89119, USA; Kumud.Acharya@dri.edu

* Correspondence: zyu@hhu.edu.cn or zhongbo.zyu@gmail.com; Tel.: +1-702-468-1539

Received: 29 October 2018; Accepted: 30 December 2018; Published: 8 January 2019



Abstract: Changes in extreme precipitation are critical to assess the potential impacts of climate change on human and natural systems. This paper provides a comprehensive investigation on the multi-scale temporal variability of extreme precipitation in the Source Region of the Yellow River (SRYP). The statistical analysis explores multi-scale extreme precipitation variability ranging from short to long term, including seasonal, annual, and inter-annual variations at different locations in the SRYP. The results suggest that seasonal patterns of extreme precipitation do not always follow the seasonal pattern of total precipitation. Heavy precipitation mostly happens during the period from May and October with July as the peak, while dry conditions are mostly seen in winter seasons. However, there are no significant annual trends for most indices at most locations. The extreme heavy precipitation presents an increasing trend at high elevation and decreasing trend at low elevation. The extreme dry condition presents more consistently decreasing trends at nearly all locations. Long-term analyses indicate that most of the selected indices except average daily intensity display multi-year bands ranging from 2 to 8 years which is probably due to the effects of El Niño–Southern Oscillation (ENSO). A further evaluation on how the ENSO events would impact extreme precipitation shows that eastern Pacific warming (EPW) and central Pacific warming (CPW) would bring less extreme heavy precipitation compared to normal years. These results can provide a beneficial reference to understand the temporal variability of extreme precipitation in the SRYP.

Keywords: multi-scale; temporal variability; extreme precipitation; ENSO; Source Region of Yellow River

1. Introduction

Extreme climate events have received increasing attention from public, government and academic communities due to their catastrophic effects on agriculture, ecology and life [1–4]. Changes in climate directly enhance precipitation extremes as global warming induces a large increase in atmospheric water vapor content which accelerates the hydrologic cycle [5–7]. As a result, changes in extreme precipitation tend to be larger than changes in mean precipitation totals either at the global scale or region scale [8,9]. Moreover, the changes in precipitation extremes are projected to continue into the future [10,11].

Previous studies indicate that both human-induced global warming and natural variability contribute to the recent extreme precipitation [12–15]. An increasing trend in the precipitation extremes has been observed over the US during the past few decades due to human-induced global warming [16]. In addition, the variation of large-scale ocean-atmospheric circulation patterns makes a non-negligible contribution to the recent high extreme precipitation values [13]. Cayan et al. [17] and

Meehl et al. [18] suggested that ENSO helps to explain the occurrence of heavy winter precipitation at inter-annual temporal scales in the western United States. Jiang et al. [14] indicated that Pacific Decadal Oscillation (PDO) and Atlantic Multi-decadal Oscillation (AMO) are also found to be associated with heavy precipitation by the modulation of PDO and the AMO cycle on the ENSO-precipitation signal. As a result, extreme precipitation may exhibit a multi-scale temporal variability due to the combined influences of human-induced warming and large-scale ocean circulations.

The source region of the Yellow River (SRYR) was selected as the study region. The SRYR contributes about 35% of the Yellow River Basin's total streamflow, which is a significant contribution to downstream water resource requirements [19–21]. However, decreasing precipitation during the monsoon period has led to a streamflow decrease and may cause further water shortage problems in the downstream area. In addition, changes in the temporal distribution of precipitation, especially precipitation extremes, may place more pressure on water resource management than changes in average precipitation totals [22–24]. As a result, it is critical to fully understand the temporal variability of extreme precipitation in the SRYR. Previous studies have mostly focused on the changes in the mean values of climatic variables at various temporal scales. Assessments of extreme precipitation are very limited and mainly investigate its annual trend. Few studies have been conducted to examine the multi-scale temporal variability of extreme precipitation in the study area. Trend and variability analyses have been applied frequently in hydro-climatic studies to investigate the impact of climate change on the selected variables. These statistical methods include the Cumulative Anomaly Curve Method [25], Mann-Kendall (MK) Nonparametric test [26], Linear/Nonlinear regression analysis, T test, and etc. [27,28]. Besides these technologies, wavelet analysis has received increasing attention and has been widely applied to many fields of hydrology to elucidate localized characteristic of non-stationary time series both in temporal and frequency domains. For instance, Goyal [29] and He and Guan [30] applied wavelet analysis to obtain the frequency bands of interest and then to forecast the evolution of rainfall and streamflow based on the statistical conclusions. Huang et al. [31], Rashid et al. [32], and Asong et al. [33] used wavelet analysis to assess the relationship between droughts and large-scale ocean oscillations with the concept of wavelet coherence [34], which reveals local similarities between two time series and could be regarded as a local correlation coefficient in the time–frequency plane. It is one of the popular and powerful methods which can detect the long- and short-term time intervals for low- and high-frequency signals, respectively [35].

In this paper, we strive to offer a comprehensive analysis of multi-scale temporal variability of extreme precipitation in the SRYR. We seek here to: (1) explore the multi-scale variability of extreme precipitation, ranging from short to long term, including seasonal, annual, inter-annual, and decadal variabilities; (2) investigate how ENSO events impact extreme precipitation; and (3) explore possible extreme precipitation scenarios for the upcoming decade based on the projected conditions of large-scale oceanic oscillations.

2. Study Area and Method

2.1. Study Area

The source region of the Yellow River is located in the northeastern Qinghai-Tibetan Plateau (Figure 1). It has a total area of 121,972 km², which covers about 15% of the Yellow River Basin. The SRYR is a mountainous region with a large elevation difference which ranges from 2670 m in the east to 6253 m in the west. The study area is dominated by a typical Qinghai-Tibetan Plateau climate system and presents a cold, semi-humid climate. Precipitation exhibits strong seasonal variability: More than 70% of the annual precipitation falls during the wet summer period (June–September) as the southwestern Asian monsoon from Bay of Bengal in the Indian Ocean brings rich moisture to the SRYR [20]. In the winter, precipitation is mainly controlled by the high pressure of the Qinghai-Tibetan Plateau; more than 78% of precipitation falls in the form of snow. However, due to the small portion of winter precipitation relative to the annual precipitation totals, snowfall accounts for

less than 10% of the annual precipitation [19,36]. Precipitation in this region presents a low intensity (<50 mm/d), long duration (1–30 days) pattern, and covers a large area (>100,000 km²). The mean annual precipitation displays a strong spatial variability, ranging from 800 mm/a in the southeast to 200 mm/a in the northwest.

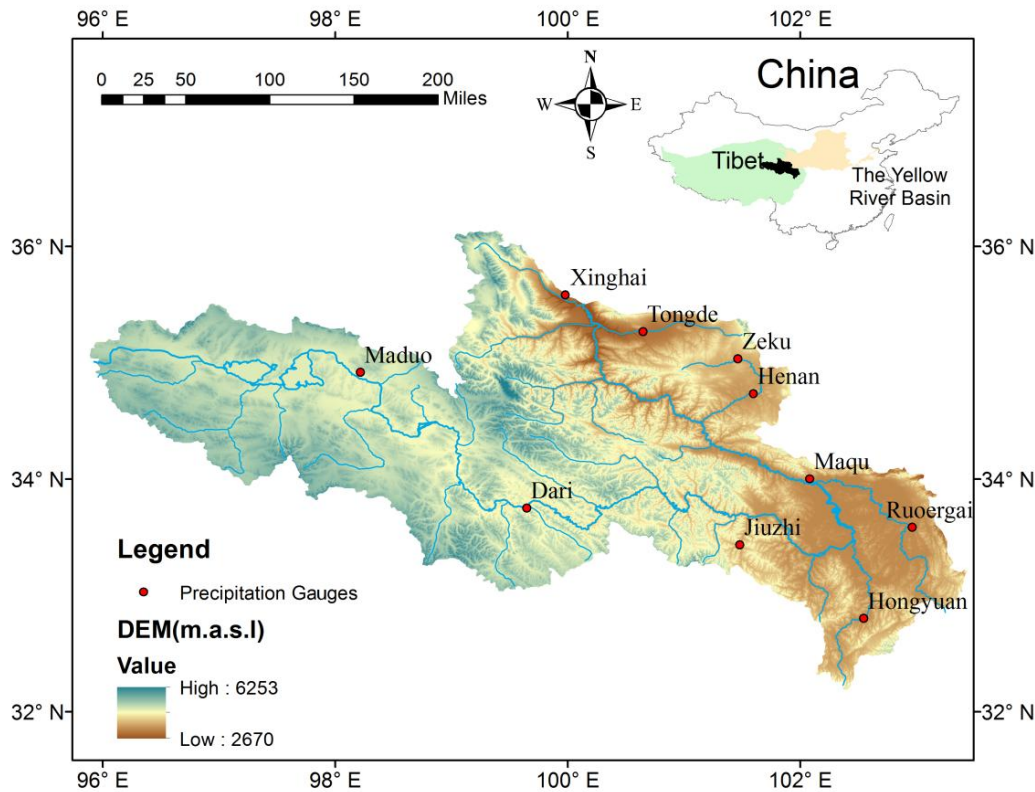


Figure 1. Map of study area with precipitation gauges.

2.2. Data and Method

Precipitation data were obtained from a dataset of daily precipitation observations from the China Meteorological Administration (CMA). This dataset is available for 743 Chinese stations covering the period from 1951–2015 and was quality checked by the National Meteorological Information Center (NMIC) of the CMA. Ten meteorological stations were selected in this study which cover the upper, middle, and lower regions of the SRYR (Figure 1). Our analysis was limited to the period from 1961 to 2015 (except Tongde and Zeku, for which data cover the period from 1961 to 2010) to avoid biases introduced by missing data. The daily precipitation data during the selected period have less than 1% missing values for all selected stations. The missing data were filled by bilinear interpolation of Tropical Rainfall Measuring Mission (TRMM) data. For the period when TRMM data were not available, ordinary kriging was chosen to interpolate nearby station data to the target station with missing values.

Six indices (Table 1) were selected for the analysis of multi-scale variability of extreme precipitation. These indices represent changes in the intensity, frequency, and duration of precipitation events. R95 is a percentile-based index for the measurement of heavy precipitation that exceeds 95 percentile thresholds. It covers, but is not limited to, most extreme precipitation events in a year [37]. R20 is a threshold index defined as the number of days when daily precipitation exceeds 20mm during the specific period. R5D belongs to absolute indices representing maximum or minimum values within a specific period. R95, R20, and R5D are regarded as heavy precipitation, which capture the tail of the distribution. SDII is an intensity index. Rather than capturing the tail of the distribution, it is more likely to show the middle of the distribution [14]. CDD belongs to duration indices representing

periods of excessive warmth, cold, wetness, or dryness. It describes the length of the longest dry period in a year and is used for the evaluation of droughts.

Table 1. Six indices of precipitation extremes as described by Frich et al. [38]¹.

Index	Definitions	Units
R20	Total count of days when RR \geq 20 mm	days
CDD	Maximum number of consecutive dry days with RR < 1 mm	days
R5D	Maximum 5-day precipitation total	mm
SDII	Total precipitation divided by the number of wet days	mm/day
R95	Total precipitation when RR > 95th percentile	mm
PRCPTOT	Total precipitation of wet days	mm

¹ Abbreviations are as follows: RR, daily precipitation. A wet day is defined when RR \geq 1 mm, and a dry day is defined when RR < 1 mm.

For the analysis of seasonal variability of extreme precipitation, the selected indices were calculated at a monthly scale. Long-term monthly average were obtained for the study period. CDD usually covers a period longer than a month; as a result, CDD was calculated annually with the start date and end date indicated in the figure.

For the analysis of the annual trend of extreme precipitation, annual extreme precipitation indices were calculated and examined by the linear regression method and the non-parametric Mann-Kendall test, which is independent of the statistical distribution of the data. Statistical significance of the trend was tested at the 0.05 level.

To explore the inter-annual and decadal extreme precipitation variability, we applied wavelet transform to examine the dominant frequency modes and the manner in which these frequency modes change over time. Wavelet analysis is generally based on one mother wavelet and can be classified as two types: discrete and continuous wavelet analysis. In this study, the continuous wavelet transform via translation and dilation of the Morlet wavelet across extreme precipitation time series was used for trend and variability analyses. Continuous wavelet transform is the convolution of the discrete series with a scaled and translated version of a wavelet $\Psi_0(\eta)$:

$$W_n(s) = \sum_{n'=0}^{N-1} x_{n'} \Psi^* \left[\frac{(n' - n)\delta t}{s} \right] \quad (1)$$

x_n : discrete sequence, δt : time spacing, s : wavelet scale, and n : localized time index.

The wavelet power spectrum of the time series is defined as:

$$P_w(\Gamma) = \left\{ |W_n(s)|^2 : s \in \Gamma \right\} \quad (2)$$

Γ : a set of scales

The Morlet wavelet is selected as the mother wavelet:

$$\Psi_0(\eta) = \pi^{-1/4} e^{i\omega_0\eta} e^{-\eta^2/2} \quad (3)$$

Additionally, we classified three types of ENSO (Table 2) using the definition proposed by Kim et al. [39]. These events were classified by the de-trended sea surface temperature (SST) anomaly index for August to October [40]. EPW is generally considered as conventional El Niño warming in the eastern Pacific region, which is defined as Niño 3 (SST region: 5° N–5° S, 150° W–90° W) warming greater than 1 standard deviation (SD). CPW refers to episodes of warming in the central Pacific region, which is defined as Niño 4 (SST region: 5° N–5° S, 160° E–150° W) warming greater than 1 SD, while Niño 3 stays below this range. East Pacific cooling (EPC) is regarded as episodes of cooling in the eastern Pacific region, which is defined as Niño 3 or Niño 3.4 (SST region: 5° N–5° S, 170° W–120° W) cooler than 1 SD. The averages of monthly extreme precipitation in the ENSO year and the year after

the ENSO year were computed and compared with the average of monthly extreme precipitation in and after the normal year. Percentages of annual extreme precipitation anomalies were calculated to examine the impacts of different ENSO events on annual extreme precipitation [41].

Table 2. Years of EPW, CPW and EPC.

ENSO Event	Years
EPW	1963, 1965, 1972, 1976, 1982, 1987, 1997
CPW	1969, 1991, 1994, 2002, 2004, 2009
EPC	1964, 1970, 1971, 1973, 1975, 1985, 1988, 1995, 1998, 1999, 2007, 2010, 2011

3. Results and Discussion

3.1. Seasonal Variability of Extreme Precipitation

Extreme heavy precipitation (represented by R95, R5D, and R20) shows a similar seasonal pattern as total precipitation at most locations (Figure 2). Extreme heavy precipitation events mostly happen between May and October with July as the peak value month at most locations. Exceptions are seen at Dari and Hongyuan, where the peak value appears in June for R5D. The ranks of the magnitude of R95 and R5D are consistent with those of monthly total precipitation regarding the locations. However, R20 displays different consistency: R20 at Ruoergai has the highest value while the total precipitation ranks 3rd among the 10 locations, which indicates that precipitation at Ruoergai exhibits a higher intensity and lower duration pattern compared with precipitation at other locations. SDII shows a similar spatial pattern with R20. However, SDII at Ruoergai, Hongyuan, Zeku, Xinghai, and Maduo present different seasonal patterns from total precipitation. In other words, the peak average daily intensity at these locations happens in the month (August) when the total precipitation is not the highest, which may due to fewer rainy days in August at these locations.

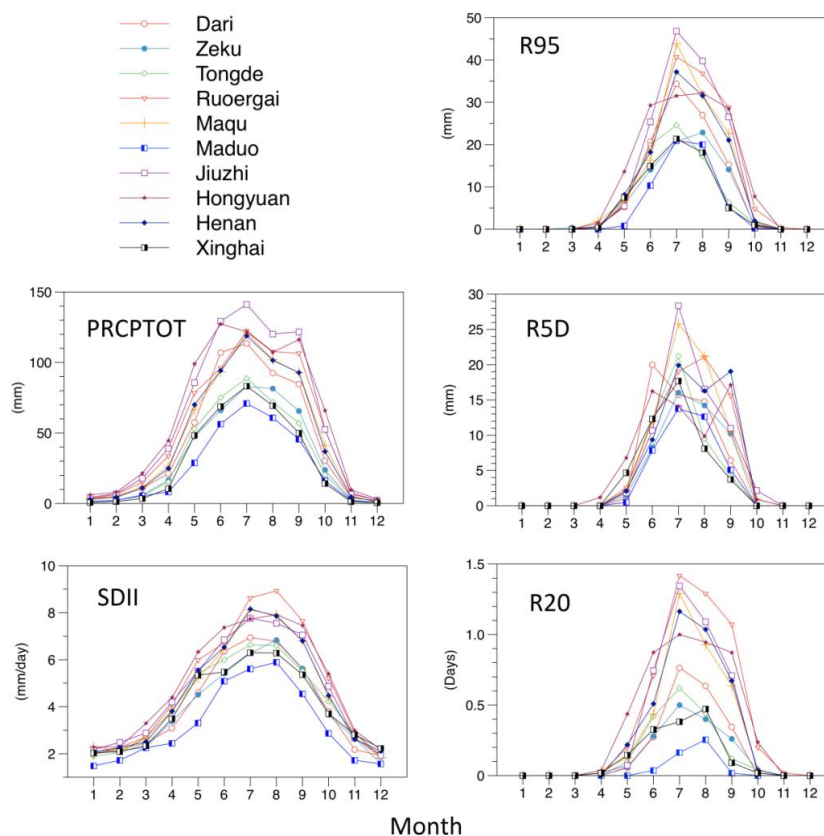


Figure 2. Long-term seasonal average of extreme precipitation indices.

The extreme dry conditions (represented by CDD) mostly happen in the winter season (Figure 3). December and January are the two months with the highest frequency for consecutive dry days. Xinghai has the longest average dry period, with 220 consecutive dry days in the historic records (Figure 4). Although the average monthly total precipitation of Maduo is the lowest, the average CDD of Maduo is much lower than that of Xinghai (ranking 4th among the 10 locations). In other words, low precipitation does not necessarily mean extreme dry conditions. An integrated analysis of extreme precipitation indices provides a more complete picture of extreme conditions.

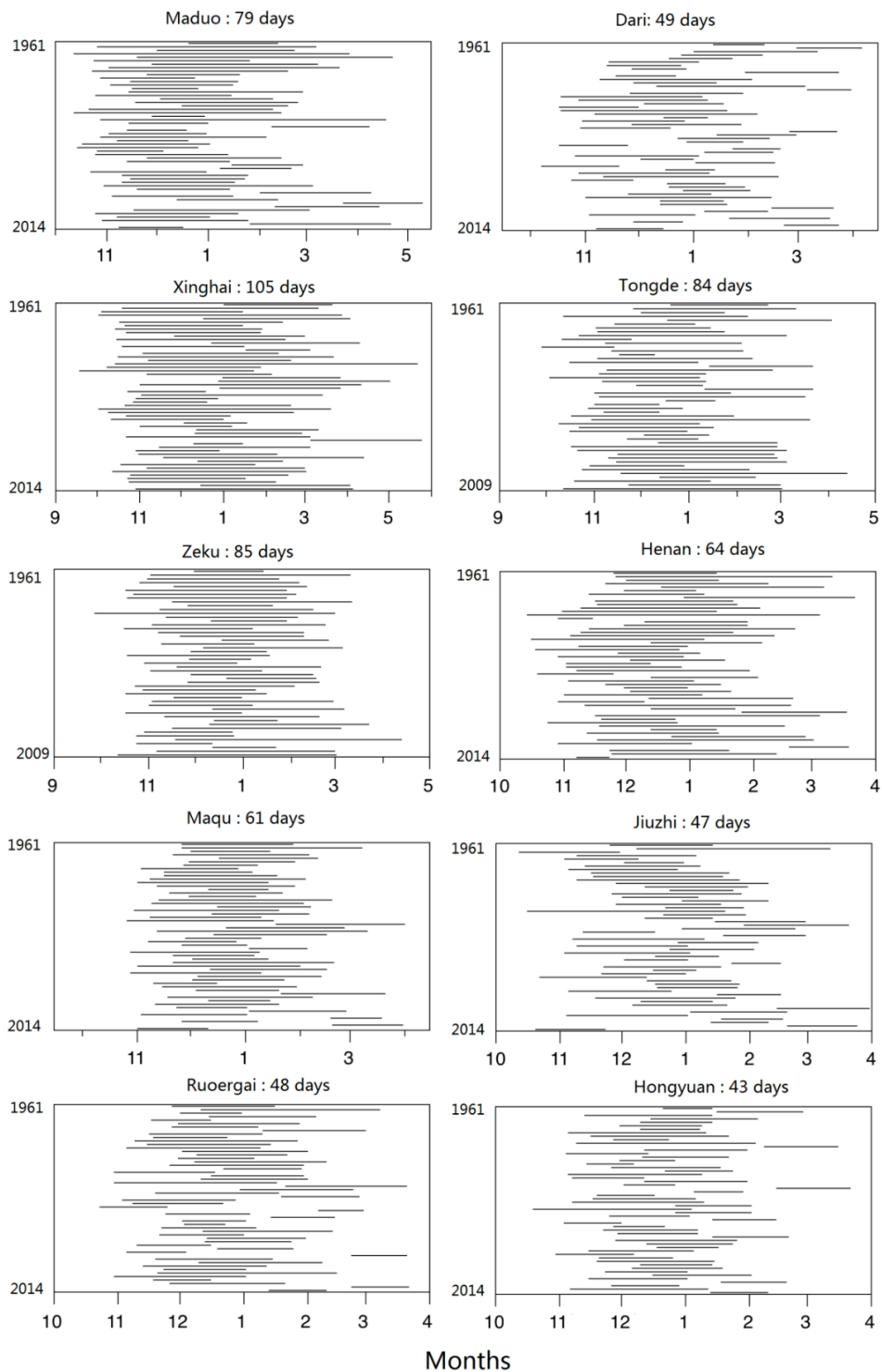


Figure 3. CDD distribution at selected locations.

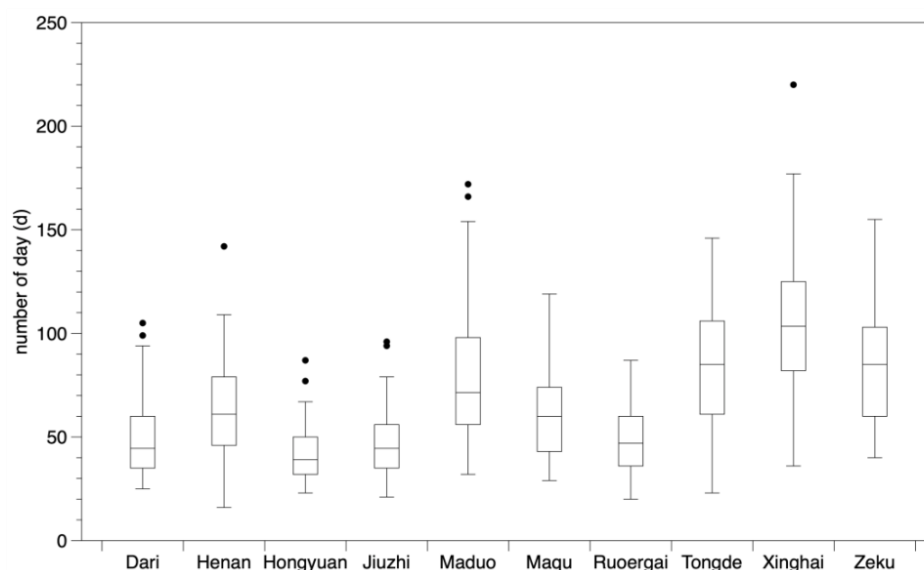


Figure 4. Boxplot of CDD at selected locations during the study period.

3.2. Annual Trend of the Extreme Precipitation

The linear trends for the extreme precipitation indices were quantified using the Mann-Kendall test (Table 3). There are no significant trends for the extreme precipitation indices at most locations except Zeku and Jiuzhi. Zeku shows a significant decreasing trend in annual total precipitation, accompanied by significantly decreasing trends in average daily intensity and extreme heavy precipitation, and a non-significantly decreasing trend in the extreme dry period. Jiuzhi exhibits significantly decreasing trends in all indices except R20, which shows a non-significantly decreasing trend. The only two significant increasing trends are seen in SDII in the Xinghai location and CDD in Tongde. SDII, R20, R95, R5D present consistent trends with PRCPTOT, which means that the extreme heavy precipitation and average daily intensity follow the trends of total precipitation. However, CDD shows more consistent decreasing trends at all locations irrespective of the total precipitation increase or decrease, which indicates that the length of the dry period becomes shorter during the study period even when the total precipitation decreases. The exception is seen in Tongde, where CDD shows a significantly increasing trend while the other extreme precipitation indices show no obvious trends. This means that the decreasing total precipitation is due to the longer dry period.

Table 3. Linear trends for the extreme precipitation at selected locations ¹.

Location	Extreme Precipitation Indices					
	SDII (mm/d/y)	R20 (d/y)	R95 (mm/y)	R5D (mm/y)	CDD (d/y)	PRCPTOT (mm/y)
Dari	0.004	0.002	0.57	0.05	−0.09	0.34
Zeku	−0.037	−0.034	−1	−0.3	−0.18	−3.32
Tongde	−0.01	−0.01	−0.9	−0.23	0.55	−1.77
Ruoergai	−0.001	−0.007	−0.14	0.01	−0.2	−1.13
Maqu	0.009	0.015	0.58	0.13	−0.18	0.67
Maduo	0.003	0.007	0.17	0.03	−0.84	1.17
Jiuzhi	−0.017	−0.028	−1.33	−0.5	−0.37	−1.34
Hongyuan	0.001	−0.025	−0.71	−0.02	−0.08	−1.01
Henan	0.002	0.005	0.05	−0.1	−0.17	−1.48
Xinghai	0.018	0.016	0.65	0.17	−0.49	1.13

¹ Bold numbers indicate the line trend is statistically significant at the 0.05 level.

3.3. Inter-Annual and Decadal Variation of the Extreme Precipitation

Figure 5 shows local and global wavelet spectra for annual regional average CDD time series. There is a strong 2–8 year band, which is possible evidence of the ENSO signals. R20 and R5D (Figures A2 and A3) also show a 15-year band, which may be caused by PDO modulation of ENSO signals [42,43]. SDII does not present significant 2–8 year bands (Figure A5), indicating that ENSO may have little effects on variability of SDII. The same conclusion was also found in the western United States [15].

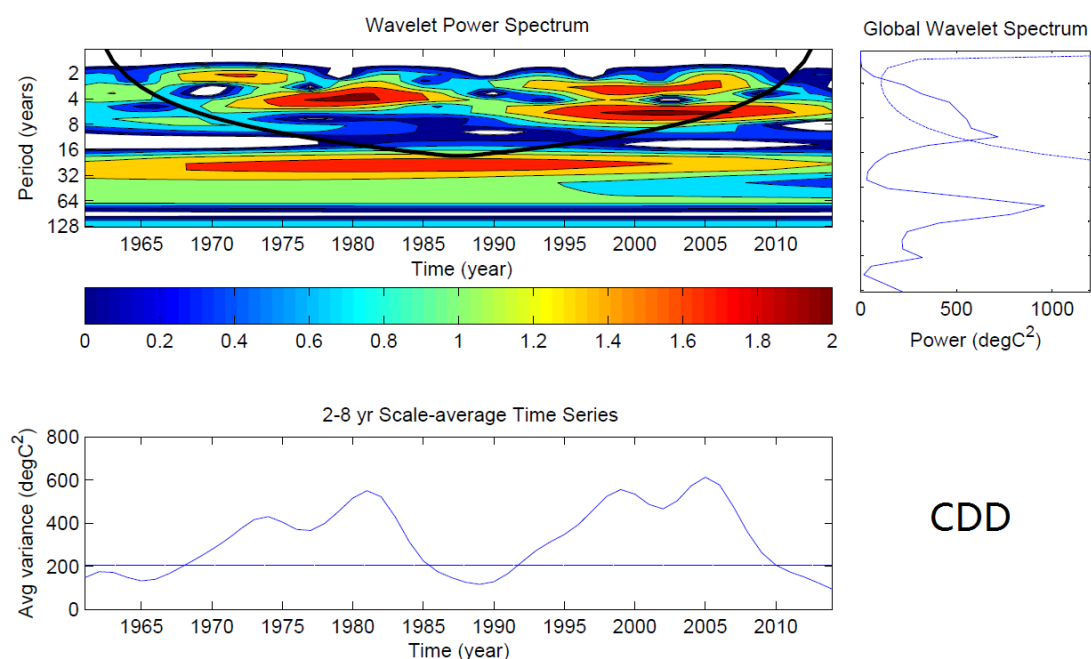


Figure 5. Local and global wavelet spectra for regional average annual CDD time series.

In order to investigate how ENSO events impact precipitation extremes, the averages of monthly extreme precipitation in an ENSO year and the year after the ENSO year were computed and compared with the average of monthly extreme precipitation in and after the normal year (Figure 6). CDD was calculated at a yearly scale; as a result, it was not included in this section. For SDII, there is no significant variation among different ENSO years and normal years, which is consistent with wavelet analysis results that ENSO may have little effects on average daily intensity in the study area. The total average precipitation is below normal during El Niño years (both EPW and CPW) especially in July, August, and September, which is consistent with the previous studies on the relationship between ENSO and average precipitation in China [44,45]. However, it is worth noting here that the abnormality of July–September precipitation during CPW is more significant than that during EPW years. The most significant differences between EPW and CPW are their different time evolution patterns and structure [46]. The CPW shifts the anomalous convection westward and causes relatively less strong westerly and southwesterly winds, thus bringing less than normal moisture to the SRYR. The seasonal pattern and the magnitude of average precipitation in EPC years are very similar to those in normal years. In the EPW year, the peak of R20 and R5D happened in August, while the peak of PRCPTOT and R95 happened in July. The peak value in the EPW year is smaller than in normal years except for R5D. In the EPC year, the peak of all selected indices happened in July and the peak values are close to the peak values in normal years. In the CPW year, the peak timing varies among different indices. The peak of R5D appears in July while the peak of R95 appears in June. R20 has two peaks, with the larger peak in June and smaller peak in August. The peak value of all indices except SDII is significantly smaller than that in normal years. The impacts of ENSO events on heavy precipitation are much larger than those on total precipitation and precipitation intensity. The peaks

of heavy precipitation indices (R20, R95, and R5D) after EPW and CPW significantly increase while EPC has a relatively small impact on the peaks of heavy precipitation indices in a year after EPC. The seasonal variability of precipitation is controlled by two major moisture source: the southern moisture which is transported by the mid-latitude westerly and the southern moisture which is related to the Indian summer monsoon [47,48]. Cao et al. [45] suggested that the strengthening of westerly and southwesterly winds in the decaying year of CPW will bring more moisture to China, compared to a developing CPW. This may explain the enhanced precipitation and heavy precipitation in a year after CPW. The decaying EPW will experience a stronger westerly and southwesterly wind but a weakened anti-cyclone compared to the developing phase. Despite the reduced moisture caused by the weakened anti-cyclone [49], there are more heavy precipitation events in the phase of the decaying EPW compared to the developing EPW. In other words, the Indian monsoon plays a more dominant role in the heavy precipitation events during EPW compared to the atmospheric circulation. Jin, et al. [50] and Timmermann, et al. [51] suggested an increased El Niño frequency in the future, especially the increasing frequency of CPW events due to various reasons such as the shoaling of the thermocline in the central Pacific region that enhances vertical exchange processes [52] and the effect on the surface layer heat balance in the northeastern subtropics caused by wind-driven advection and surface heat fluxes [53]. The heavy precipitation events may decrease from the aspect of oceanic circulation.

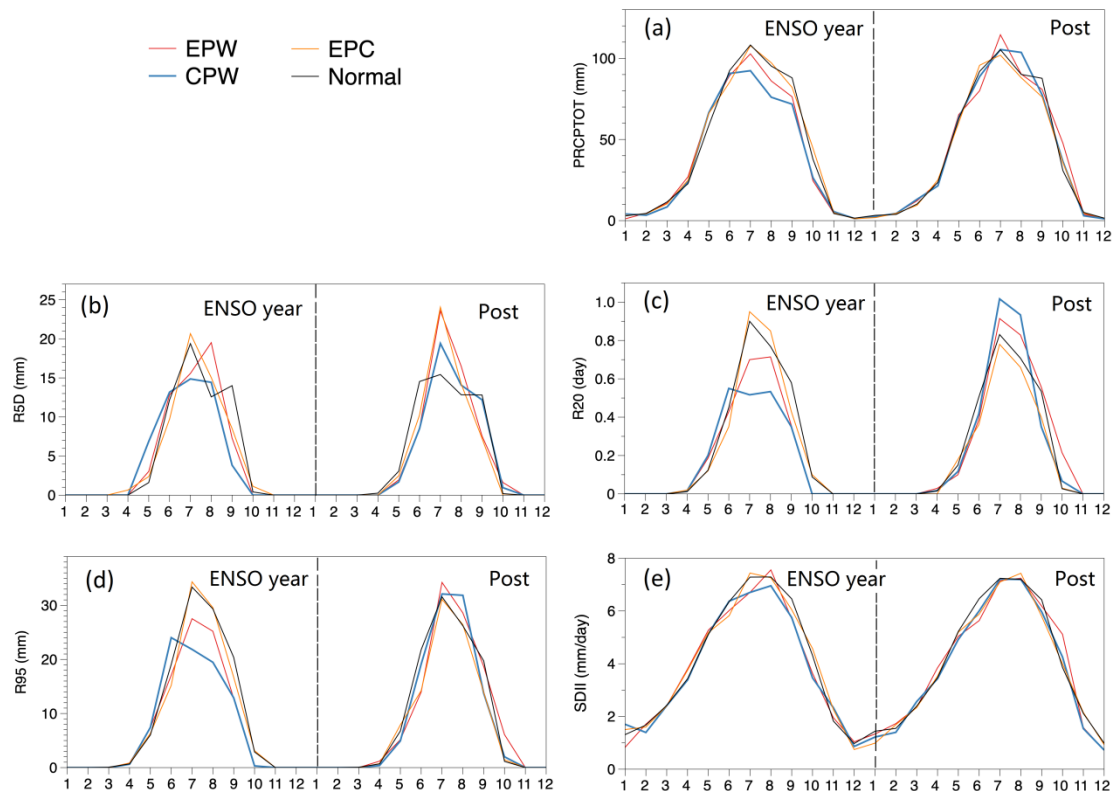


Figure 6. Monthly extreme precipitation indices in and after an ENSO year. (a) represents SDII; (b) represents PRCPTOT (total precipitation); (c) represents R95; (d) represents R5D; (e) represents R20.

4. Conclusions

In this study, we have investigated the multi-scale variability of extreme precipitation including heavy precipitation indices (R20, R5D, and R95), drought indices (CDD), intensity indices (SDII), and total precipitation (PRCPTOT) in the SRYR. We base our analyses on different temporal scales ranging from short-term to long-term (seasonal, annual, and inter-annual) variations. Our analysis indicates that the magnitude of heavy precipitation varies among locations, and the spatial variation of heavy precipitation generally follows the spatial variation of total precipitation. However, it is worth noting

that a higher precipitation amount does not always mean a higher intensity event. Ruergai has higher average daily intensity and more days with precipitation higher than 20mm while its total precipitation is not the highest among the selected locations. Heavy precipitation mostly happens during the period from May and October with July as the peak at most locations. Dry conditions are mostly seen in winter seasons. There are no significant annual trends for the selected heavy precipitation indices at most locations except Zeku and Jiuzhi, where significant negative trends are observed. Extreme dry conditions show negative trends at most locations except Tongde. The annual trends of intensity indices and heavy precipitation indices are mostly positive at higher elevations and negative at lower elevations. For the long-term variations, the selected indices excluding SDII are impacted by ENSO. The impacts of ENSO events on heavy precipitation are much larger than those on total precipitation and precipitation intensity. During EPW and CPW years, the extreme heavy precipitation is significantly less than normal and in the year after the EPW and CPW year. Based on the projected increasing El Niño frequency, extreme heavy precipitation may decrease from the aspect of oceanic circulation.

Author Contributions: Conceptualization, P.J., Z.Y., and K.A.; Methodology, P.J.; Data curation, P.J. and F.Y.; writing—original draft preparation, P.J.; writing—review and editing, Z.Y. and K.A.

Funding: This work was supported by the National Key R&D Program of China (Grant No. 2016YFC0402710); National Natural Science Foundation of China (Grant No. 51539003, 41761134090); National Science Funds for Creative Research Groups of China (No. 51421006); and Open Research Fund Program of State Key Laboratory of Hydrology-Water Resources and Hydraulic Engineering (Grant No. 2015490611).

Acknowledgments: This research was made possible by the generosity and support of the Sulo and Aileen Maki Endowment. The authors acknowledge that the views herein are that of the authors only and do not necessarily reflect the review of the funding agencies and the organizations they are affiliated with.

Conflicts of Interest: The authors declare no conflict of interest.

Appendix A

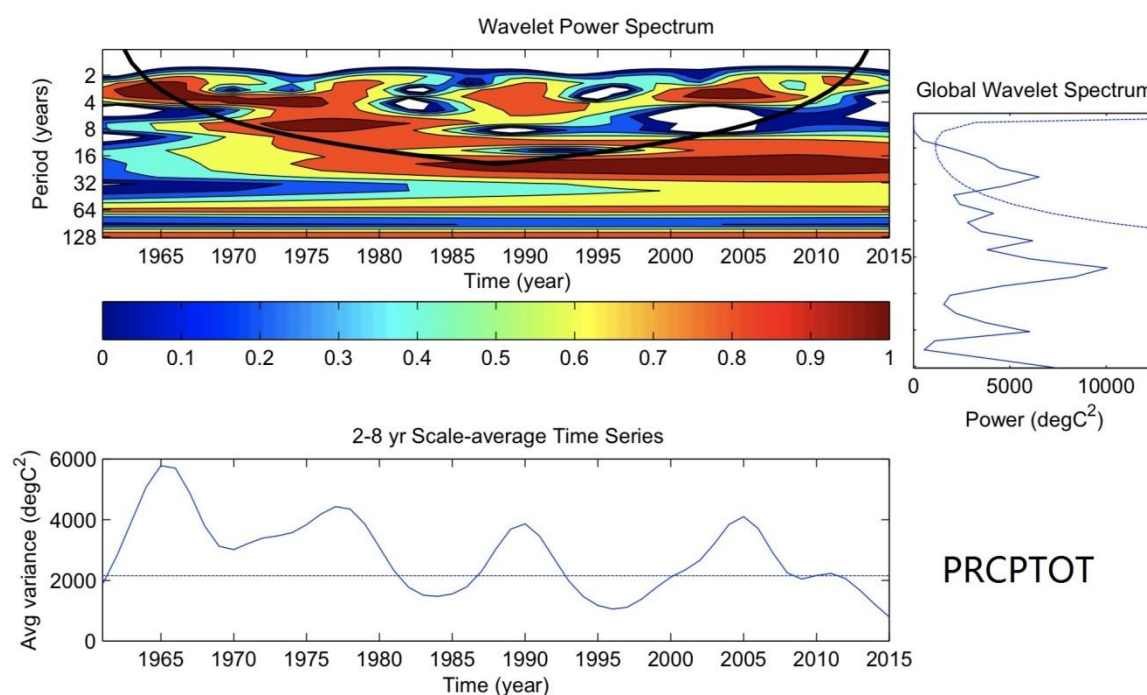


Figure A1. Local and global wavelet spectra for regional average annual PRCPTOT time series.

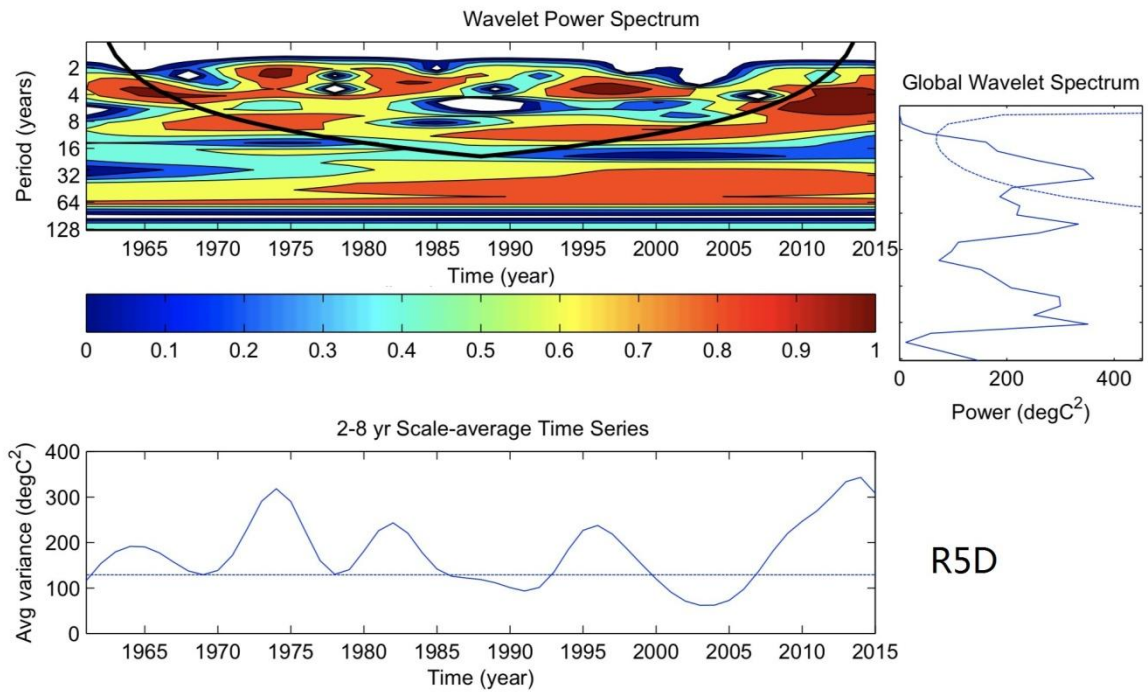


Figure A2. Local and global wavelet spectra for regional average annual R5D time series.

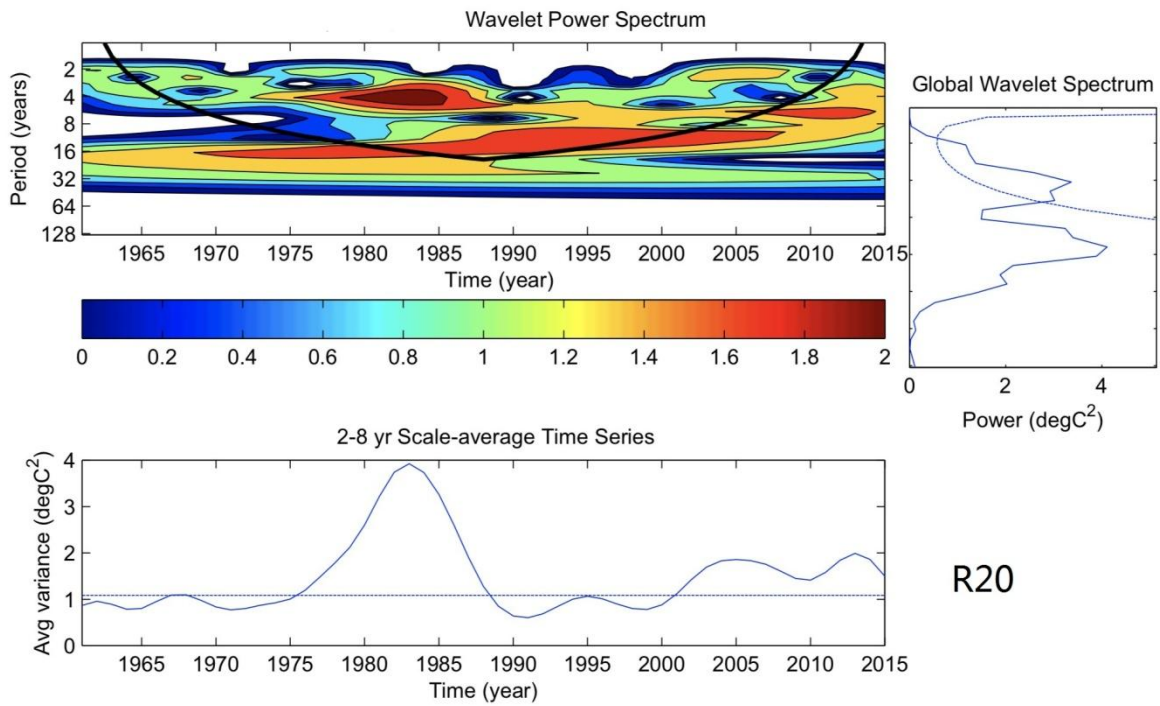


Figure A3. Local and global wavelet spectra for regional average annual R20 time series.

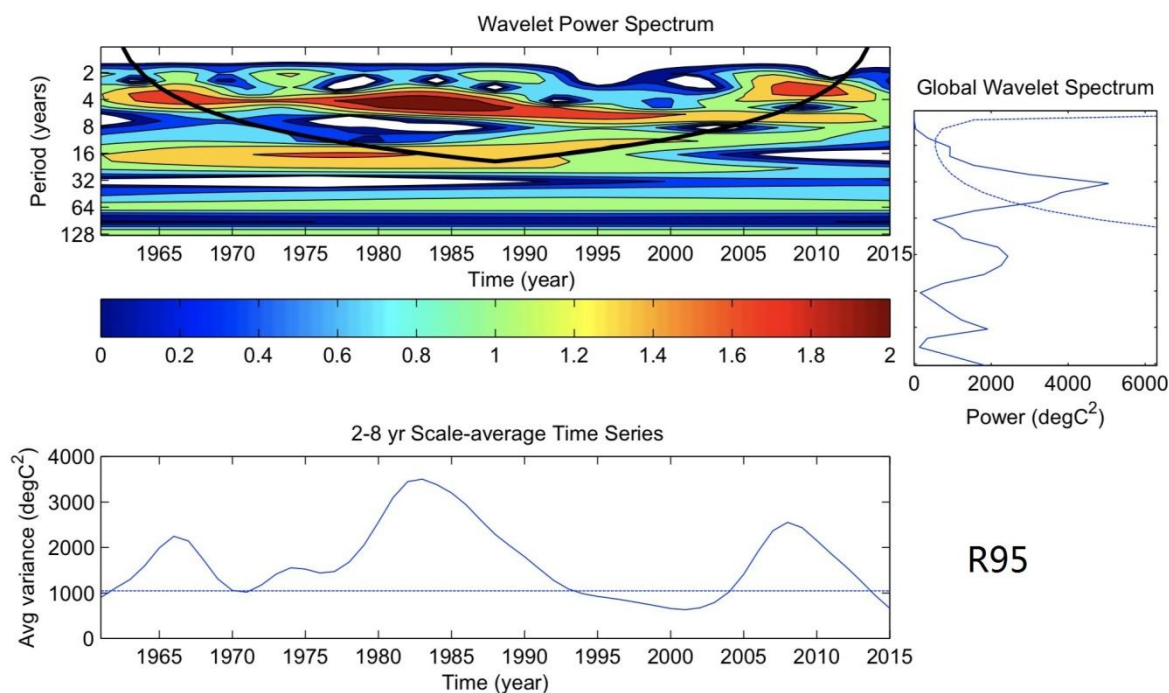


Figure A4. Local and global wavelet spectra for regional average annual R95 time series.

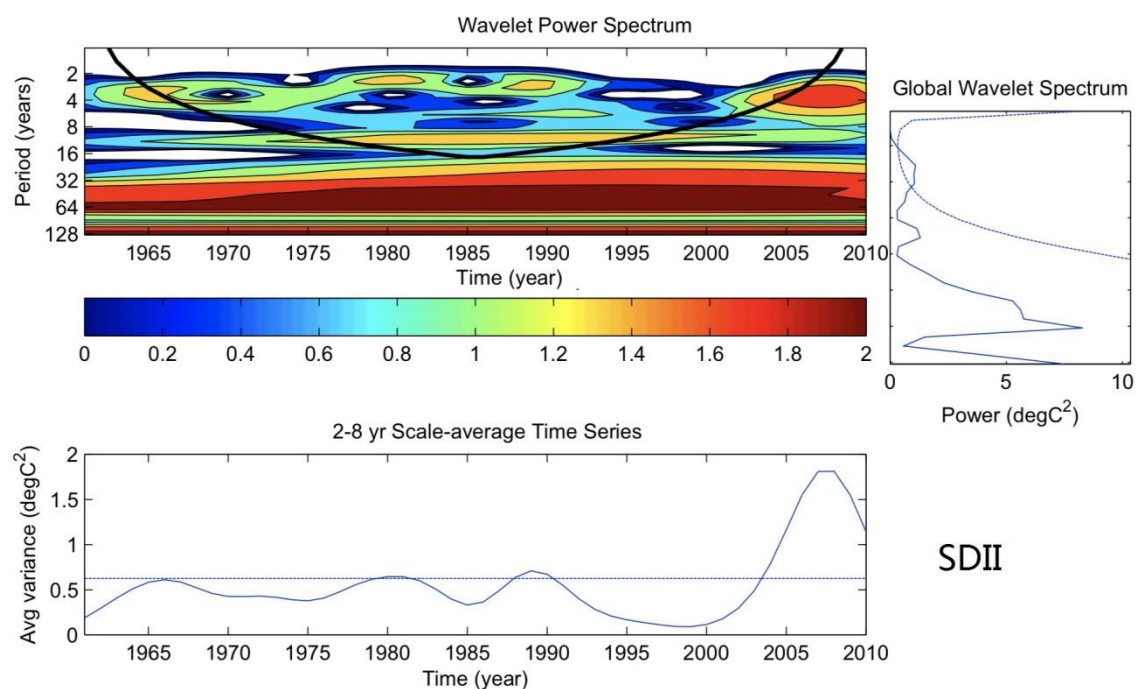


Figure A5. Local and global wavelet spectra for regional average annual SDII time series.

References

1. Fu, G.; Yu, J.; Yu, X.; Ouyang, R.; Zhang, Y.; Wang, P.; Liu, W.; Min, L. Temporal variation of extreme rainfall events in China, 1961–2009. *J. Hydrol.* **2013**, *487*, 48–59. [[CrossRef](#)]
2. Penalba, O.C.; Robledo, F.A. Spatial and temporal variability of the frequency of extreme daily rainfall regime in the La Plata Basin during the 20th century. *Clim. Chang.* **2010**, *98*, 531–550. [[CrossRef](#)]
3. You, Q.; Kang, S.; Aguilar, E.; Yan, Y. Changes in daily climate extremes in the eastern and central Tibetan Plateau during 1961–2005. *J. Geophys. Res.* **2008**, *113*. [[CrossRef](#)]

4. Peng, Y.; Zhao, X.; Wu, D.; Tang, B.; Xu, P.; Du, X.; Wang, H. Spatiotemporal variability in extreme precipitation in China from observations and projections. *Water* **2018**, *10*, 1089. [[CrossRef](#)]
5. Allen, M.R.; Ingram, W.J. Constraints on future changes in climate and the hydrologic cycle. *Nature* **2002**, *419*, 224–232. [[CrossRef](#)] [[PubMed](#)]
6. Meehl, G.A.; Zwiers, F.; Evans, J.; Knutson, T.; Mearns, L.; Whetton, P. Trends in extreme weather and climate events: Issues related to modeling extremes in projections of future climate change. *Bull. Am. Meteorol. Soc.* **2000**, *81*, 427–436. [[CrossRef](#)]
7. Semenov, V.; Bengtsson, L. Secular trends in daily precipitation characteristics: Greenhouse gas simulation with a coupled AOGCM. *Clim. Dyn.* **2002**, *19*, 123–140.
8. Groisman, P.Y.; Knight, R.W.; Easterling, D.R.; Karl, T.R.; Hegerl, G.C.; Razuvaev, V.N. Trends in intense precipitation in the climate record. *J. Clim.* **2005**, *18*, 1326–1350. [[CrossRef](#)]
9. Hu, Y.; Maskey, S.; Uhlenbrook, S. Trends in temperature and rainfall extremes in the Yellow River source region, China. *Clim. Chang.* **2012**, *110*, 403–429. [[CrossRef](#)]
10. Klein Tank, A.; Peterson, T.; Quadir, D.; Dorji, S.; Zou, X.; Tang, H.; Santhosh, K.; Joshi, U.; Jaswal, A.; Kolli, R. Changes in daily temperature and precipitation extremes in central and South Asia. *J. Geophys. Res.* **2006**, *111*. [[CrossRef](#)]
11. Song, X.; Song, S.; Sun, W.; Mu, X.; Wang, S.; Li, J.; Li, Y. Recent changes in extreme precipitation and drought over the Songhua River basin, China, during 1960–2013. *Atmos. Res.* **2015**, *157*, 137–152. [[CrossRef](#)]
12. Min, S.-K.; Zhang, X.; Zwiers, F.W.; Hegerl, G.C. Human contribution to more-intense precipitation extremes. *Nature* **2011**, *470*, 378–381. [[CrossRef](#)] [[PubMed](#)]
13. Kunkel, K.E.; Easterling, D.R.; Redmond, K.; Hubbard, K. Temporal variations of extreme precipitation events in the United States: 1895–2000. *Geophys. Res. Lett.* **2003**, *30*. [[CrossRef](#)]
14. Jiang, P.; Yu, Z.; Gautam, M.R. Pacific and Atlantic Ocean influence on the spatiotemporal variability of heavy precipitation in the western United States. *Glob. Planet. Chang.* **2013**, *109*, 38–45.
15. Jiang, P.; Yu, Z.; Gautam, M.R.; Acharya, K. The spatiotemporal characteristics of extreme precipitation events in the western United States. *Water Resour. Manag.* **2016**, *30*, 4807–4821. [[CrossRef](#)]
16. Zhang, X.; Zwiers, F.W.; Hegerl, G.C.; Lambert, F.H.; Gillett, N.P.; Solomon, S.; Stott, P.A.; Nozawa, T. Detection of human influence on twentieth-century precipitation trends. *Nature* **2007**, *448*, 461–465. [[CrossRef](#)] [[PubMed](#)]
17. Cayan, D.R.; Redmond, K.T.; Riddle, L.G. Enso and hydrologic extremes in the western United States. *J. Clim.* **1999**, *12*, 2881–2893. [[CrossRef](#)]
18. Meehl, G.A.; Tebaldi, C.; Teng, H.; Peterson, T.C. Current and future us weather extremes and El Niño. *Geophys. Res. Lett.* **2007**, *34*. [[CrossRef](#)]
19. Yuan, F.; Berndtsson, R.; Uvo, C.B.; Zhang, L.; Jiang, P. Summer precipitation prediction in the source region of the Yellow River using climate indices. *Hydrol. Res.* **2016**, *47*, 847–856. [[CrossRef](#)]
20. Hu, Y.; Maskey, S.; Uhlenbrook, S.; Zhao, H. Streamflow trends and climate linkages in the source region of the Yellow River, China. *Hydrol. Process.* **2011**, *25*, 3399–3411. [[CrossRef](#)]
21. Zheng, H.; Zhang, L.; Liu, C.; Shao, Q.; Fukushima, Y. Changes in stream flow regime in headwater catchments of the Yellow River basin since the 1950s. *Hydrol. Process.* **2007**, *21*, 886–893. [[CrossRef](#)]
22. Katz, R.W.; Brown, B.G. Extreme events in a changing climate: Variability is more important than averages. *Clim. Chang.* **1992**, *21*, 289–302. [[CrossRef](#)]
23. Taniguchi, K. Future changes in precipitation and water resources for Kanto region in Japan after application of pseudo global warming method and dynamical downscaling. *J. Hydrol.* **2016**, *8*, 287–303. [[CrossRef](#)]
24. Afzal, M.; Gagnon, A.S.; Mansell, M.G. The impact of the variability and periodicity of rainfall on surface water supply systems in Scotland. *J. Water Clim. Chang.* **2016**, *7*, 321–339. [[CrossRef](#)]
25. Yang, Y.; Yang, J.-K.; Miao, Q.-S.; Gao, X.-M. The interannual trend and preliminary quantitative estimation of the oceans condition in the Bohai Sea area. In *IOP Conference Series: Earth and Environmental Science*; IOP Publishing: Bristol, UK, 2017; p. 012061.
26. Yue, S.; Wang, C. The mann-kendall test modified by effective sample size to detect trend in serially correlated hydrological series. *Water Resour. Manag.* **2004**, *18*, 201–218. [[CrossRef](#)]
27. Xiao, Z.; Shi, P.; Jiang, P.; Hu, J.; Qu, S.; Chen, X.; Chen, Y.; Dai, Y.; Wang, J. The spatiotemporal variations of runoff in the Yangtze River basin under climate change. *Adv. Meteorol.* **2018**, *2018*, 5903451. [[CrossRef](#)]

28. Partal, T.; Kahya, E. Trend analysis in Turkish precipitation data. *Hydrol. Process.* **2006**, *20*, 2011–2026. [[CrossRef](#)]
29. Goyal, M.K. Monthly rainfall prediction using wavelet regression and neural network: An analysis of 1901–2002 data, Assam, India. *Theor. Appl. Climatol.* **2014**, *118*, 25–34. [[CrossRef](#)]
30. He, X.; Guan, H. Multiresolution analysis of precipitation teleconnections with large-scale climate signals: A case study in South Australia. *Water Resour. Res.* **2013**, *49*, 6995–7008. [[CrossRef](#)]
31. Liu, S.; Huang, S.; Huang, Q.; Xie, Y.; Leng, G.; Luan, J.; Song, X.; Wei, X.; Li, X. Identification of the non-stationarity of extreme precipitation events and correlations with large-scale ocean-atmospheric circulation patterns: A case study in the Wei River basin, China. *J. Hydrol.* **2017**, *548*, 184–195. [[CrossRef](#)]
32. Rashid, M.M.; Johnson, F.; Sharma, A. Identifying sustained drought anomalies in hydrological records: A wavelet approach. *J. Geophys. Res.* **2018**, *123*, 7416–7432. [[CrossRef](#)]
33. Asong, Z.E.; Wheeler, H.S.; Bonsal, B.; Razavi, S.; Kurkute, S. Historical drought patterns over Canada and their teleconnections with large-scale climate signals. *Hydrol. Earth Syst. Sci.* **2018**, *22*, 3105–3124. [[CrossRef](#)]
34. Grinsted, A.; Moore, J.C.; Jevrejeva, S. Application of the cross wavelet transform and wavelet coherence to geophysical time series. *Nonlinear Process. Geophys.* **2004**, *11*, 561–566. [[CrossRef](#)]
35. Mehr, A.D.; Kahya, E.; Olyae, E. Streamflow prediction using linear genetic programming in comparison with a neuro-wavelet technique. *J. Hydrol.* **2013**, *505*, 240–249. [[CrossRef](#)]
36. Hu, Y.; Maskey, S.; Uhlenbrook, S. Downscaling daily precipitation over the Yellow River source region in china: A comparison of three statistical downscaling methods. *Theor. Appl. Climatol.* **2013**, *112*, 447–460. [[CrossRef](#)]
37. Alexander, L.; Zhang, X.; Peterson, T.; Caesar, J.; Gleason, B.; Tank, A.K.; Haylock, M.; Collins, D.; Trewin, B.; Rahimzadeh, F. Global observed changes in daily climate extremes of temperature and precipitation. *J. Geophys. Res.* **2006**, *111*. [[CrossRef](#)]
38. Frich, P.; Alexander, L.V.; Della-Marta, P.; Gleason, B.; Haylock, M.; Tank, A.K.; Peterson, T. Observed coherent changes in climatic extremes during the second half of the twentieth century. *Clim. Res.* **2002**, *19*, 193–212. [[CrossRef](#)]
39. Kim, H.-M.; Webster, P.J.; Curry, J.A. Impact of shifting patterns of Pacific Ocean warming on North Atlantic tropical cyclones. *Science* **2009**, *325*, 77–80. [[CrossRef](#)]
40. Smith, T.M.; Reynolds, R.W. Improved extended reconstruction of SST (1854–1997). *J. Clim.* **2004**, *17*, 2466–2477. [[CrossRef](#)]
41. Zhang, Q.; Li, J.; Singh, V.P.; Xu, C.Y.; Deng, J. Influence of ENSO on precipitation in the East River basin, South China. *J. Geophys. Res.* **2013**, *118*, 2207–2219. [[CrossRef](#)]
42. Xue, X.; Chen, W.; Chen, S.; Feng, J. PDO modulation of the ENSO impact on the summer South Asian high. *Clim. Dyn.* **2018**, *50*, 1393–1411. [[CrossRef](#)]
43. Jiang, P.; Gautam, M.R.; Zhu, J.; Yu, Z. How well do the GCMS/RCMS capture the multi-scale temporal variability of precipitation in the southwestern United States? *J. Hydrol.* **2013**, *479*, 75–85. [[CrossRef](#)]
44. Chan, J.C.; Zhou, W. PDO, ENSO and the early summer monsoon rainfall over south China. *Geophys. Res. Lett.* **2005**, *32*. [[CrossRef](#)]
45. Cao, Q.; Hao, Z.; Yuan, F.; Su, Z.; Berndtsson, R.; Hao, J.; Nyima, T. Impact of enso regimes on developing-and decaying-phase precipitation during rainy season in China. *Hydrol. Earth Syst. Sci.* **2017**, *21*, 5415–5426. [[CrossRef](#)]
46. Xiang, B.; Wang, B.; Li, T. A new paradigm for the predominance of standing central Pacific warming after the late 1990s. *Clim. Dyn.* **2013**, *41*, 327–340. [[CrossRef](#)]
47. Xu, X.; Zhao, T.; Lu, C.; Guo, Y.; Chen, B.; Liu, R.; Li, Y.; Shi, X. An important mechanism sustaining the atmospheric “water tower” over the Tibetan Plateau. *Atmos. Chem. Phys.* **2014**, *14*, 11287–11295. [[CrossRef](#)]
48. Li, Q.; Yang, M.; Wan, G.; Wang, X. Spatial and temporal precipitation variability in the source region of the Yellow River. *Environ. Earth Sci.* **2016**, *75*, 594. [[CrossRef](#)]
49. Feng, J.; Chen, W.; Tam, C.Y.; Zhou, W. Different impacts of El Niño and El Niño modoki on China rainfall in the decaying phases. *Int. J. Climatol.* **2011**, *31*, 2091–2101. [[CrossRef](#)]
50. Jin, F.F.; An, S.I.; Timmermann, A.; Zhao, J. Strong El Niño events and nonlinear dynamical heating. *Geophys. Res. Lett.* **2003**, *30*, 20–21. [[CrossRef](#)]
51. Timmermann, A.; Oberhuber, J.; Bacher, A.; Esch, M.; Latif, M.; Roeckner, E. Increased El Niño frequency in a climate model forced by future greenhouse warming. *Nature* **1999**, *398*, 694–697. [[CrossRef](#)]

52. Yeh, S.-W.; Kug, J.-S.; Dewitte, B.; Kwon, M.-H.; Kirtman, B.P.; Jin, F.-F. El Niño in a changing climate. *Nature* **2009**, *461*, 511–514. [[CrossRef](#)] [[PubMed](#)]
53. Yu, J.-Y.; Kao, H.-Y.; Lee, T. Subtropics-related interannual sea surface temperature variability in the central equatorial Pacific. *J. Clim.* **2010**, *23*, 2869–2884. [[CrossRef](#)]



© 2019 by the authors. Licensee MDPI, Basel, Switzerland. This article is an open access article distributed under the terms and conditions of the Creative Commons Attribution (CC BY) license (<http://creativecommons.org/licenses/by/4.0/>).